remote sensing

MDPI

Article

Cascading Machine Learning to Monitor Volcanic Thermal Activity Using Orbital Infrared Data: From Detection to Quantitative Evaluation

Simona Cariello [1,2], Claudia Corradino [2,*], Federica Torrisi [1,2] and Ciro Del Negro [2]

[1] Department of Electrical Electronics and Computer Engineering, University of Catania, 95125 Catania, Italy; simona.cariello@ingv.it (S.C.); federica.torrisi@ingv.it (F.T.)
[2] Istituto Nazionale di Geofisica e Vulcanologia, Sezione di Catania, Osservatorio Etneo, 95125 Catania, Italy; ciro.delnegro@ingv.it
* Correspondence: claudia.corradino@ingv.it

Abstract: Several satellite missions are currently available to provide thermal infrared data at different spatial resolutions and revisit time. Furthermore, new missions are planned thus enabling to keep a nearly continuous 'eye' on thermal volcanic activity around the world. This massive volume of data requires the development of artificial intelligence (AI) techniques for the automatic processing of satellite data in order to extract significant information about volcano conditions in a short time. Here, we propose a robust machine learning approach to accurately detect, recognize and quantify high-temperature volcanic features using Sentinel-2 MultiSpectral Instrument (S2-MSI) imagery. We use the entire archive of high spatial resolution satellite data containing more than 6000 S2-MSI scenes at ten different volcanoes around the world. Combining a 'top-down' cascading architecture, two different machine learning models, a scene classifier (SqueezeNet) and a pixel-based segmentation model (random forest), we achieved a very high accuracy, namely 95%. These results show that the cascading approach can be applied in near-real time to any available satellite image, providing a full description of the scene, with an important contribution to the monitoring, mapping and characterization of volcanic thermal features.

Keywords: volcano; satellite remote sensing; cascading ensemble technique; transfer learning; Sentinel 2-MSI

Citation: Cariello, S.; Corradino, C.; Torrisi, F.; Del Negro, C. Cascading Machine Learning to Monitor Volcanic Thermal Activity Using Orbital Infrared Data: From Detection to Quantitative Evaluation. *Remote Sens.* **2024**, *16*, 171. https://doi.org/10.3390/rs16010171

Academic Editor: José Fernández

Received: 17 October 2023
Revised: 22 December 2023
Accepted: 27 December 2023
Published: 31 December 2023

1. Introduction

The continuous advances in remote sensing thermal imaging and the growing capacity of artificial intelligence (AI) techniques bring extraordinary opportunities for volcano monitoring, which can directly benefit from automatic procedures to process huge amounts of satellite data. Using AI in operational monitoring centers like the Etna Volcano Observatory (EVO) may accelerate the response to volcanic hazardous events, as massively large raw thermal images can be turned into useful information on the status of the volcanic activity in a short time. Measuring the temporal thermal behavior of active volcanoes improves our understanding of volcanic processes. Remote sensing of high-temperature volcanic features offers a means of documenting the ongoing eruption, while yielding insights on potential volcanic hazards [1–3]. Indeed, active volcanoes are often dangerous for close-range monitoring and regular visual observations, and thermal measurements are impractical, especially when an eruption is ongoing. Different satellite monitoring systems have been developed to capture thermal features due to changes in the temperature of crater lakes, emplacement of hot material along the flanks of volcanoes or ejection of ash and gas into the atmosphere [4]. Being able to promptly detect and recognize the type of volcanic activity taking place, as well as quantify the erupted products, is fundamental for volcanic hazard assessment in near-real time. Over the past decades, thermal infrared

remote sensing observations have been effective in achieving extensive improvements in volcano monitoring from space. In particular, thermal infrared satellite-based sensors have been exploited to locate and monitor high-temperature volcanic phenomena, from the detection and mapping of active lava flows, lakes and tubes, to the analyses of structural, fumarolic and crater lake features [2]. Generally speaking, volcanic features with different sizes and temperatures may be investigated using a number of satellite sensors at different spatial, spectral and temporal resolutions [5–7]. High spatial resolution satellite sensors allow achieving finer spectral and geometric details of the observed volcanic phenomena, thus allowing to visually recognize the type of volcanic activity taking place, e.g., extended thermal anomalies due to effusive activity such as lava lakes and lava flows, or isolated thermal anomalies due to degassing, intra-crater eruptive activity and volcanic explosions. A range of hot spot dimension and radiance characteristics can in effect be assessed to make an interpretation and assign the volcanic hot spot a label. The main volcanic hot spot types are defined by typical spatial attributes (shape, size, pattern, texture, site, and/or association) and/or spectral attributes (brightness) defining a feature type that can be used to assign each volcanic hot spot to a unique category [2]. An obvious qualitative route to determining the feature type with which the hot spot is associated is to assess the basic hot spot dimension and brightness (radiance). The characteristic size, shape, radiance intensity, pattern, and, most importantly, association of the component parts, allow most of the features to be identified and distinguished at a glance using the trained eye. The abundance of image collections acquired from numerous orbital sensors is leading to a critical need for novel approaches to process these large datasets, thereby overcoming the limits of visual inspection and traditional approaches, e.g., fixed threshold-based techniques [8–10]. To date, artificial intelligence (AI) techniques represent the fastest-growing trend in remote sensing data analysis applications relying on the availability of massive volumes of data. AI is the branch of computer science aimed at building automated systems capable of retrieving meaningful information from data, using approaches that would traditionally require elements of decision making and intelligence [11,12]. Machine learning (ML) and deep learning (DL) are the two main fields of AI in which algorithms can improve their performance through learning and exploiting training sample data [11]. The potentiality of ML and DL algorithms in recognizing volcanic features in optical and radar satellite images has already been tested. Recent studies have shown that AI can overcome the drawbacks of existing threshold-based approaches for satellite-based volcano features detection owing to its ability to find more complex and precise relationships among thresholds [13,14]. The ML tasks already achieved in volcanology using satellite thermal data include identifying and mapping the thermal emissions from active and cooling lava flows [7,15]; estimating the areal coverage and the total volume of lava fields or deposits [16]; and detecting and characterizing the main components of volcanic plumes during explosive eruptions [17]. DL is widely used in computer vision to train a model to automatically catch spatial and spectral attributes from images and recognize its content. We successfully applied DL algorithms to automatically recognize subtle to intense thermal anomalies exploiting the spatial relationships of the volcanic features [18].

Designing an accurate ML model with a high generalization capability is a challenging task. To this end, ensemble architectures can be used to reduce classification errors by using multiple ML models to obtain better predictive performance than could be obtained from any of its constituents. Cascades are a subset of ensembles, but they execute the collected models sequentially, by merging the solutions once the prediction has a high enough confidence in order to have a great degree of certainty in the prediction [19–21]. These models, exploiting high computational power and a large amount of data, can be easily implemented using cloud computing platforms. Cloud computing is now widely used in several scientific fields, enabling a wide range of users to access distributed, scalable, virtualized hardware and/or software infrastructure over the Internet [22,23]. Multi-petabyte catalogs of satellite imagery and geospatial datasets are already stored in public data archives and readily accessible. Here, we present a cascading pipeline to classify

the high-temperature volcanic features and quantify the spatial extension of the thermal anomalies from high spatial resolution satellite data. Unique to this algorithm is its ability to achieve extremely high accuracy by combining, in a 'top-down' cascading architecture, two different ML models, a scene classifier and a pixel-based segmentation model. On the one hand, we exploit the potentiality of DL SqueezeNet (SN) to associate a global class to each **scene** based on both spatial and spectral features. This approach has already been shown to be effective in detecting the presence of eruptive activity in different volcanoes around the world [24]. The step forward proposed here is using the potentiality of DL in automatically learning spatial and spectral attributes from images to distinguish the type of volcanic activity as either isolated volcanic thermal anomalies, due for instance to intra-crater activity, degassing, new vent opening, explosive activity or extended volcanic effusive activity, including lava lakes, lava domes and lava flows. Furthermore, non-active volcanic scenes (non-erupting volcanoes) are more specifically recognized based on the atmospheric condition, distinguishing between clear-sky and cloudy-sky conditions. Thus, four classes are considered, namely 'Isolated Volcanic Thermal Anomalies' (*ITA*), 'Extended Volcanic Thermal Anomalies' (*ETA*), 'No Volcanic Activity' (*NVA*) and 'Cloudy-Sky Condition' (*CSC*). On the other hand, an ML random forest is adopted to achieve two main tasks, namely to improve the SN classification using an ensemble cascading architecture and to accurately map thermal anomalies at pixel scale using spectral features. We investigated the potential of our approach by analyzing the entire S2-MSI archive containing about 6000 S2-MSI scenes at ten different volcanoes around the world. The cascading model was developed using both Google Earth Engine (GEE), a cloud-based platform for satellite data analysis [25], and Google Colaboratory (Colab), a cloud platform hosted by Google to program in Python, for data analysis, statistics, machine learning and deep learning applications [26].

2. Materials

2.1. Volcanoes Selection

We investigated ten volcanoes located in different areas around the world in order to account for heterogeneity in our dataset (see in Figure 1): Kilauea (Hawaii, USA), Cumbre Vieja (Canary Islands, Spain), Shiveluch (Kamchatka, Russia), Pacaya (City of Guatemala, Guatemala), Erta Ale (Afar, Ethiopia), Ambrym (Vanuatu, SW Pacific), Stromboli (Italy), Popocatépetl (Mexico), Klyuchevskaya (Kamchatka, Russia), and Etna (Italy). These volcanoes were selected for their wide variety of eruptive styles and time recurrence of eruptions between 2015 and 2023.

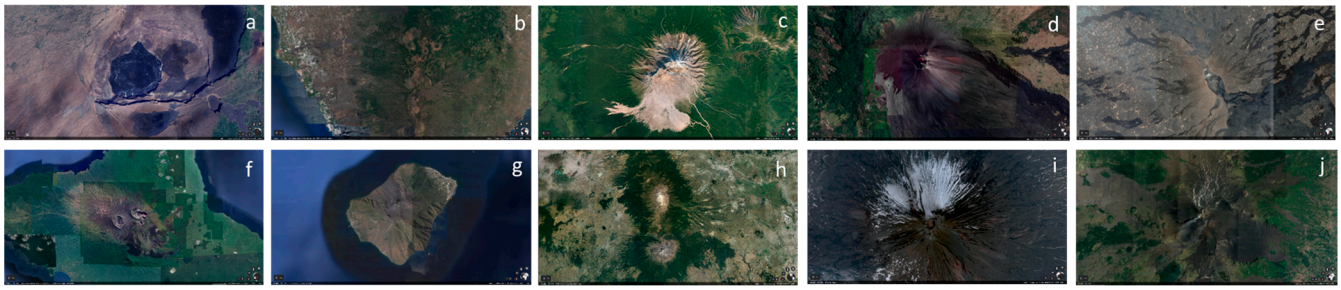

Figure 1. Volcanoes investigated: (**a**) Kilauea (Hawaii, USA), (**b**) Cumbre Vieja (Canary Islands, Spain), (**c**) Shiveluch (Kamchatka, Russia), (**d**) Pacaya (Guatemala), (**e**) Erta Ale (Afar, Ethiopia), (**f**) Ambrym (Vanuatu, SW Pacific), (**g**) Stromboli (Italy), (**h**) Popocatépetl (Mexico), (**i**) Klyuchevskaya (Kamchatka, Russia), and (**j**) Etna (Italy). All the images were captured via Google Earth Pro [http://www.earth.google.com (accessed on 14 October 2023)].

Kīlauea (Figure 1a) is the youngest volcano in Hawaii and one of the world's most active volcanoes, with frequent summit and flank lava flow eruptions interspersed with periods of long-term lava lake activity at Halemaumau Crater in the summit caldera.

Cumbre Vieja (Figure 1b) is a volcanic ridge located on the island of La Palma in the Canary Islands, Spain. It is known for its potential volcanic activity and the significant impact it could have on the surrounding region due to its unstable geology and is characterized by explosive activity and lava flows.

Shiveluch (Figure 1c) is one of the most active and prominent volcanoes in the Kamchatka Peninsula of Russia's Far East. It is part of the larger Kamchatka volcanic complex and is known for its frequent and sometimes explosive volcanic activity characterized by lava dome formations.

Pacaya (Figure 1d) is a highly active stratovolcano located in Guatemala, Central America. It is one of the most active volcanoes in the country and is known for its frequent eruptions and stunning lava displays. It has Strombolian activity, but occasional Plinian eruptions also occur.

Erta Ale (Figure 1e) is a unique and active shield volcano located in the Afar Region of Ethiopia. It is renowned for its persistent lava lake and is one of the most continuously active volcanoes in the world.

Ambrym (Figure 1f) is an active shield volcano located on the island of Ambrym in the Vanuatu archipelago in the South Pacific. It is well known for its persistent and spectacular lava lakes within its calderas, making it one of the most famous and actively monitored volcanoes in the region.

Stromboli (Figure 1g) is located on the small island of Stromboli in the Tyrrhenian Sea, part of the Aeolian Islands in Italy. It is known for its nearly constant explosive eruptions, but lava flows do occur at times. Strombolian activity represents the main hazard for the close to the crater terrace within the Sciara del Fuoco.

Popocatépetl (Figure 1h), located in the Trans-Mexican Volcanic Belt, is an active andesite–dacite stratovolcano. Gas emissions, occasionally with minor ash concentrations, occur nearly daily.

Klyuchevskaya (Figure 1i) is part of the Kamchatka volcanic complex and the larger Pacific Ring of Fire, known for its frequent eruptions and its dynamic impact on the surrounding region. It is characterized by frequent moderate-volume explosive and effusive eruptions. In October 2020, an eruption lasting five months started with Strombolian activity, explosions, lava flows and ash plumes. A new activity phase began again in November 2022, with a new eruptive phase characterized by lava fountains and ash plumes.

Etna (Figure 1j), located on the island of Sicily in Italy, is Europe's highest and most active volcano, known for its frequent eruptions, majestic beauty and historical significance. Its eruptive episodes are mainly characterized by the emission of lava fountains, pyroclastic material and lava flows.

2.2. Satellite Data

The Copernicus Sentinel-2 mission comprises a constellation of two polar-orbiting satellites placed in the same sun-synchronous orbit, phased at 180° to each other. Sentinel-2A (S2A) and Sentinel-2B (S2B) were launched in 2015 and 2017, respectively. The revisit frequency of one satellite is 10 days, resulting in a global revisit frequency of 5 days. Both satellites are equipped with a MultiSpectral Instrument (MSI) with 13 bands at 10 m spatial resolution in the visible and near-infrared, at 20 m spatial resolution in the red edge and shortwave infrared part of the spectrum, and at 60 m spatial resolution in the atmospheric bands. In Google Earth Engine, Sentinel-2 MSI images are available at different product levels. We chose to use the Level-1C archive from 2015, containing about 6000 images available as 13 UINT16 spectral bands representing TOA reflectance scaled by 10,000 (see the Sentinel-2 User Handbook for details). We used Harmonized Sentinel-2 MSI data and processed them using GEE in the bands from visible to short-infrared (VIS1:B2 with 0.496 μm (S2A)/0.492 μm (S2B) wavelength, VIS2: B3 with 0.56 μm (S2A)/0.55 μm (S2B), and VIS3: B4 with 0.66 μm (S2A, S2B)), near-infrared (NIR: B8 with 0.84 μm (S2A)/0.83 μm (S2B) wavelength), and short-wave infrared (SWIR: B11, with 1.61 μm (S2A, S2B) wavelength, and 12, with 2.20 μm (S2A)/2.19 μm (S2B) wavelength).

The default region of interest (ROI) for each volcano is one square [1 × 1] km centered at the volcano summit [27], but if necessary, the ROI can be expanded. For each acquisition, a false RGB image is created as input for the image classifier using (NIR, SWIR1, SWIR2) TOA data, then normalized using a z-score [28] and converted into a [224,224,3].jpg format (in the 0–255 scale). A subset of 1700 images is selected from the entire collection and then split into training, validation and test dataset, i.e., 60% training set, 10% validation set and 30% test set [24]. The selection criteria were used to build a balanced target dataset with half of its scenes containing volcanic activity related to active flows or erupting vents (scenes with both isolated and extended thermal anomalies) and the other half with no volcanic activity related to a volcano at rest or presence of significant cloud coverage (scenes with no thermal anomalies). Specifically, we chose representative images for each class as listed in Table 1 and shown in Figure 2 where a sample Sentinel 2 - MSI image for each class is reported. The images labelled '*CSC*' (Cloudy-Sky Condition) include scenes partially/totally obscured by thin/thick clouds where the eventual presence of thermal anomalies associated with eruptive activity was hidden by clouds. The images labelled '*NVA*' (No Volcanic Activity) include volcanic areas without thermal anomalies and clear-sky conditions. The images labelled '*ITA*' (Isolated Volcanic Thermal Anomalies) include cloudy/clear scenes where isolated hot spots are distinctly visible and these include intra-crater activity, new vent formation and explosive activity. The images labelled '*ETA*' (Extended Volcanic Thermal Anomalies) include cloudy/clear scenes where spatially extended thermal anomalies, including lava domes, lava lakes, active/cooling lava flows and lava flows fragmented by clouds, are clearly visible.

Table 1. Classes description.

CLASSES	DESCRIPTION
No Volcanic Activity [NVA]	Clear scenes without any thermal volcanic activity
Isolated Volcanic Thermal Anomalies [ITA]	Any scene containing isolated, spatially confined thermal anomalies
Extended Volcanic Thermal Anomalies [ETA]	Any scene containing distributed, spatially extended thermal anomalies
Cloudy-Sky Condition [CSC]	Scenes partially/totally containing clouds where eventual thermal anomalies are obscured

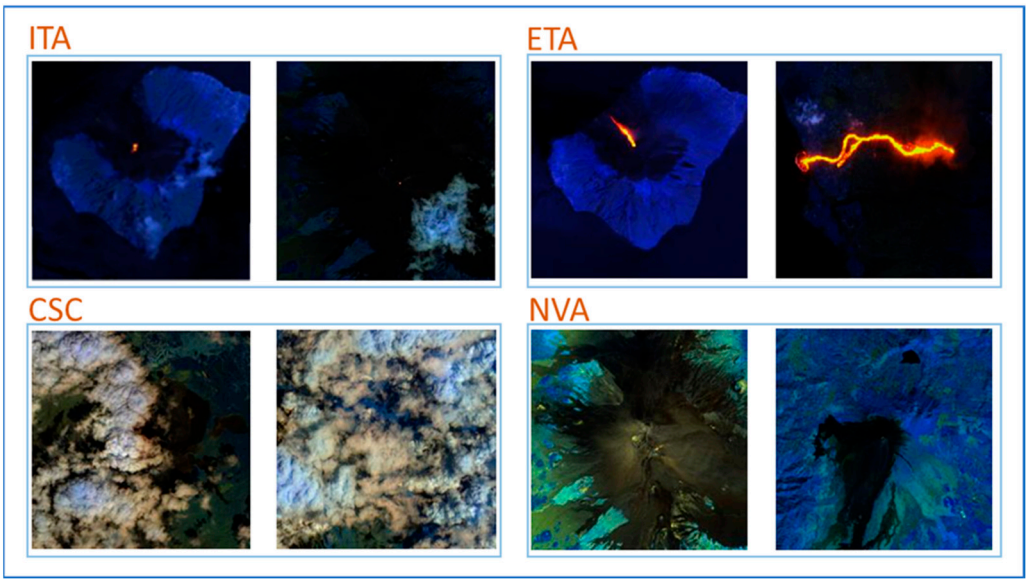

Figure 2. Sentinel 2- MSI Dataset example. Isolated Volcanic Thermal Anomalies (*ITA*), Extended Volcanic Thermal anomalies (*ETA*), No Volcanic Activity (*NVA*), Cloudy-Sky Condition (*CSC*).

Every image was assigned a label via careful analysis of the status of activity of each volcano, using information from volcanological bulletins (e.g., from the Smithsonian Institution, Global Volcanism Program, available online: https://volcano.si.edu/ (accessed on 10 September 2023), or from INGV National Institute of Geophysics and Volcanology, available online: https://www.ct.ingv.it (accessed on 10 September 2023)) and via manual inspection of the scenes. In the same way, we defined the 'ground truth' labels (i.e., the real labels of the scenes), either by examining the volcanological bulletins or manually inspecting the scenes. Thus, we have obtained a final labelled dataset composed of about 1700 images belonging to the 10 different volcanoes investigated (Kilauea, Cumbre Vieja, Shiveluch, Pacaya, Erta Ale, Ambrym, Stromboli, Popocatépetl, Klyuchevskaya and Etna), with images acquired during the years from 2016 to 2023.

3. Materials

We adopted cascading machine learning to automatically detect and recognize the volcanic thermal activity from Sentinel 2-MSI images and quantify the spatial extension of thermal anomalies. This approach used thermal infrared satellite observations not only to detect volcanic unrest based on the presence of thermal anomalies at a specific time, but also to identify numerous volcanic features based on their thermal and geometric characteristics, namely the type of volcanic thermal activity between the classes *ITA* and *ETA*.

Our cascading approach involved two steps (Figure 3). The first used the volcanic dataset to re-train eleven SqueezeNet models by applying the transfer learning approach and combined their outcomes using an ensemble approach. The second step used a random forest model, pre-trained for detecting volcanic hot spots in Sentinel-2 MSI images [13], to check the reliability of the SqueezeNet outcomes, and quantify spatially the thermal anomalies if any. These two steps are described in more detail below.

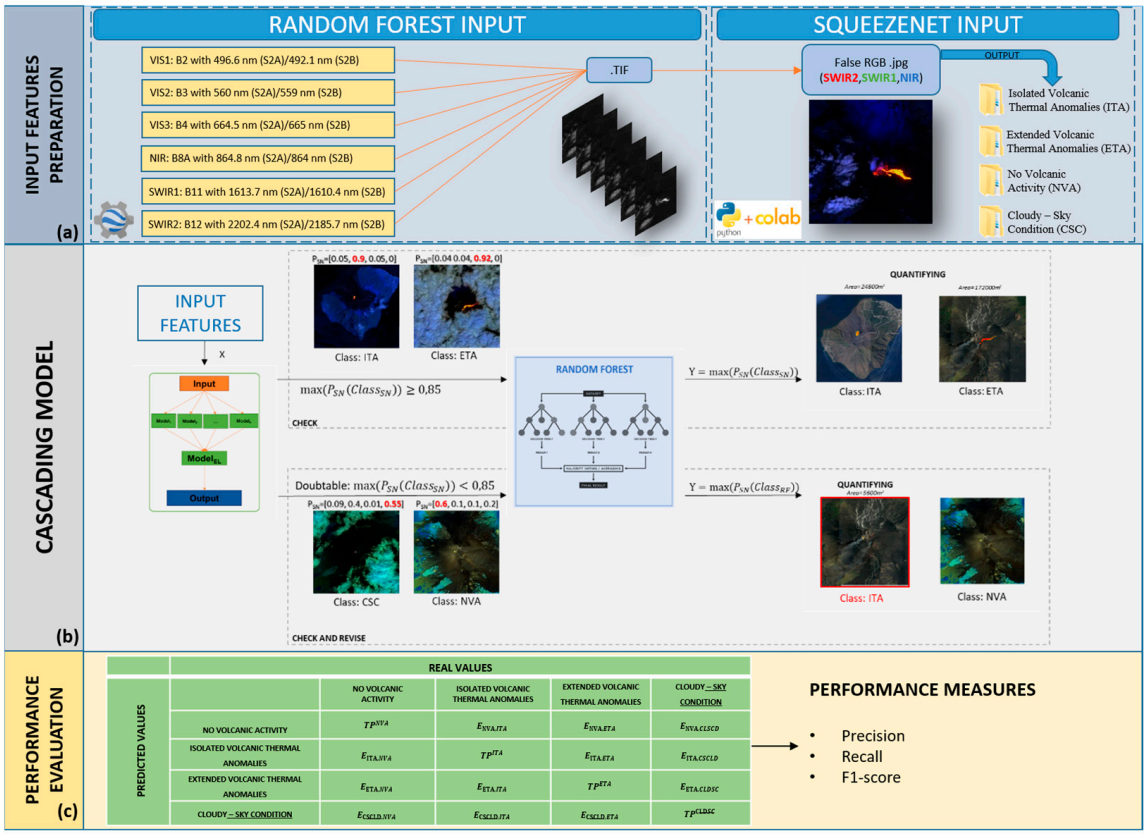

Figure 3. General scheme representing the three main steps of the cascading machine learning models: (**a**) Input feature preparation, (**b**) Cascading model and (**c**) Performance evaluation.

3.1. SqueezeNet Classifier

We used the SqueezeNet (SN) classifier to automatically detect the presence of high-temperature anomalies related to volcanic activity and recognize volcanic features in different scenes. SqueezeNet is a deep CNN model, usually used for computer vision [29], which requires far fewer parameters, thus reducing memory constraints and maintaining competitive accuracy. The main peculiarity of this CNN is the presence of Fire modules that are squeeze convolution layers with only 1 × 1 filters (Figure 4). These layers were then fed into an expand layer with a mix of 1 × 1 and 3 × 3 convolution filters [30]. This model was pre-trained on the ImageNet dataset [31], which is composed of around 14 million annotated images belonging to 1000 different classes. The SqueezeNet model trained with this dataset achieves a good balance between training time and classification accuracy [29,32].

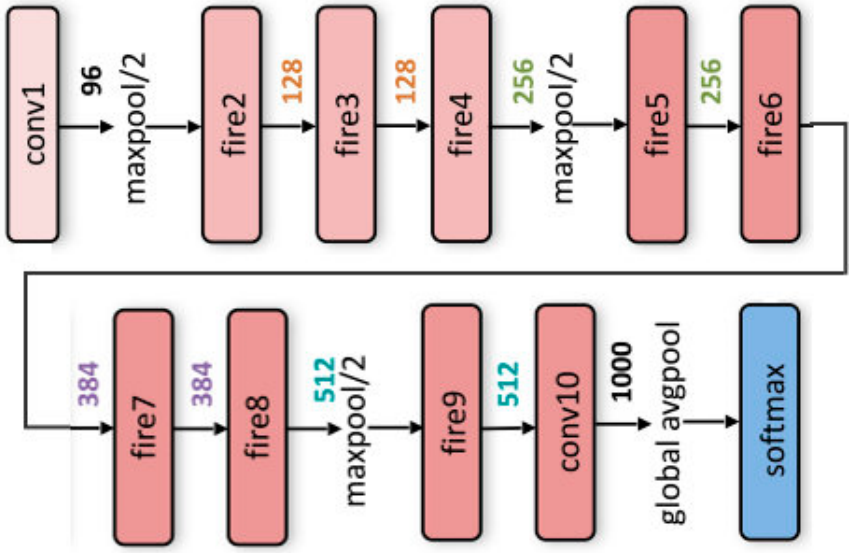

Figure 4. SqueezeNet architecture.

We applied the transfer learning approach to readjust the parameters of the pre-trained SqueezeNet model to accomplish our task. The transfer learning technique allowed us to exploit the knowledge previously acquired by the pre-trained model to a new domain, thus avoiding the use of a huge set of labeled training data and reducing training times.

The new image dataset contained scenes representative of four different types of volcanic thermal activity: isolated thermal anomalies (*ITA*), extended thermal anomalies (*ETA*), no thermal anomaly (*NVA*), and presence of cloud cover (*CSC*). Then, we combined eleven different SqueezeNet models to obtain a final SN Ensemble Classifier enhancing the global accuracy and generalization capabilities. We built the volcanic dataset, sampling 240 false RGB images and labeling them with a class specific ID. We indexed the class '*NVA*' with ID 0, the class '*ITA*' with ID 1, the class '*ETA*' with ID 2 and the class '*CSC*' with ID 3. We obtained a final balanced dataset accounting for the 10 volcanoes investigated.

The volcanic dataset was randomly split into three independent subsets: a training set, a validation set and a test set. The training set was used, in general, to train the model; the second one was used to validate the results in the training phase and to fit the hyperparameters. The last set was used to test the model and to calculate the predictive performances of the model. We fed the train and validation sets to the SqueezeNet 1.0 model in Google Colab, applying the transfer learning approach, running the model with a learning rate alpha of 0.001, a batch size of 25 and 5 epochs for the fine-tuning [11]. The number of epochs was chosen as a good trade-off between the complexity of the algorithm and goodness of the model, because a higher number of epochs did not improve the performance as much compared to the complexity. Finally, we ran the trained SqueezeNet

model a total of 10 times over the test subset (30% of the volcanic dataset). An ensemble strategy, combining the 11 trained SqueezeNet models, was the final model outcome given by the most voted one by the eleven runs of the trained model. Ensemble methods use multiple models to achieve better predictive performance than could be obtained from any of the constituent models alone [33]. Therefore, from the output vector containing the probability achieved for each class ($Class_{SN}$) namely $P_{SN} = [P_{NVA}, P_{ITA}, P_{ETA}, P_{CSC}]$, the final SN prediction would be the class with the highest probability, i.e., $\max(P_{SN}(Class_{SN}))$.

3.2. Random Forest

We used the random forest (RF) model to map low to extreme thermal anomalies using TOA reflectance Bands VIS1, VIS2, VIS3, NIR, SWIR1 and SWIR2, already trained in [13]. The strength of the RF model lies in its capacity to exploit all the spectral bands ranging from visible to short infrared, which are relevant in the detection of thermal anomalies [13]. Random forest or random decision forest classifier is an ensemble model made of multiple decision trees [34]. The decision tree is a supervised ML model able to make predictions based on simple decision rules inferred from input features during the training phase. For segmentation tasks, the output of the random forest is a map of the same dimension of the input image, where each pixel is assigned to the class 'voted' by most decision trees [34,35]. It has been widely used as a tool to detect anomalies because the separation between anomalies and normal behavior is made easier due to the shortest path in the trees than normal instances. In particular, we chose to use this model because it has been shown to have high accuracy, i.e., 0.91, being able to detect lower to high intensity changes. RF, rather than a single decision tree, allows us to reduce overfitting, to improve generalization, since the subset of the training samples is used for each tree, and to enhance stability, since the final outcome is based on several of the decision tree outcomes. The RF output is a binary map whose pixels are 0 if assigned to the background and 1 if assigned to thermal anomalies.

3.3. Cascading Machine Learning

We decided to use a cascading of machine learning models to obtain a more robust and accurate classification of the analyzed scene, reducing as much as possible the detection of false negatives [19]. Using the outputs of the two different models (SN and RF), we built a more detailed and reliable description of the scene. In particular, since a segmentation model provides finer details (e.g., isolated thermal anomalies can be detected even for scenes containing clouds), we used a check and revise block integrating a pixel-based classifier RF. Therefore, the cascading architecture allowed us to extract the maximum information content from the images by combining both the scene-based and pixel-based classifier schemes. It consisted of a top-down structure, an information processing strategy also known as stepwise design and stepwise refinement.

It started with the general big picture and then broke down from there into smaller segments and details. As previously stated, SN assigned a probability score for each class, and the predicted class corresponded to the one with the highest value. We assumed that the prediction was reliable if it was greater than a given probability threshold (TH). Therefore, when this happened, the scene classification would be exclusively based on the SN, and the random forest model would only be used to segment the image classified as either '*ITA*' or '*ETA*' and thus quantify the detected area. Conversely, when the SN probability outcome was less than TH, the check and revise block would be activated, and the RF would be used for the scene classification. In the event that at least one pixel was identified as an anomaly, this means that the scene contained either isolated or extended thermal anomalies, and thus the candidate classes ($Class_{RF}$) would be '*ITA*' and '*ETA*'. On the other hand, in the event that no pixels were detected using RF, the candidate classes would be '*CSC*' and '*NVA*'. Therefore, between the two potential $Class_{RF}$, the final prediction would be the one with the highest SN probability score, i.e., $\max(P_{SN}(Class_{RF}))$.

The sensitivity threshold TH was chosen in order to optimize the combined use of the SN block and the check and revise block, thus guaranteeing a high final cascading accuracy. Higher values meant that the cascading model was mainly reliant on the SN and vice versa; lower values meant that it was mainly reliant on the RF. Thus, it was possible to compute the accuracy of the SN block as the accuracy of the testing subset when only the SN block was active, the accuracy of the RF-based block as the accuracy of the testing subset when the 'check and revise' block was active and finally, the overall accuracy considering the overall cascading model. Figure 5 shows how the accuracy of each active block changed by changing the TH value. The value of TH = 0.85 was chosen because it optimized the performances of the two blocks, reaching the maximum accuracy values for both and higher cascading accuracy before a plateau started, i.e., for TH = 0.9 the metrics continued to be the same.

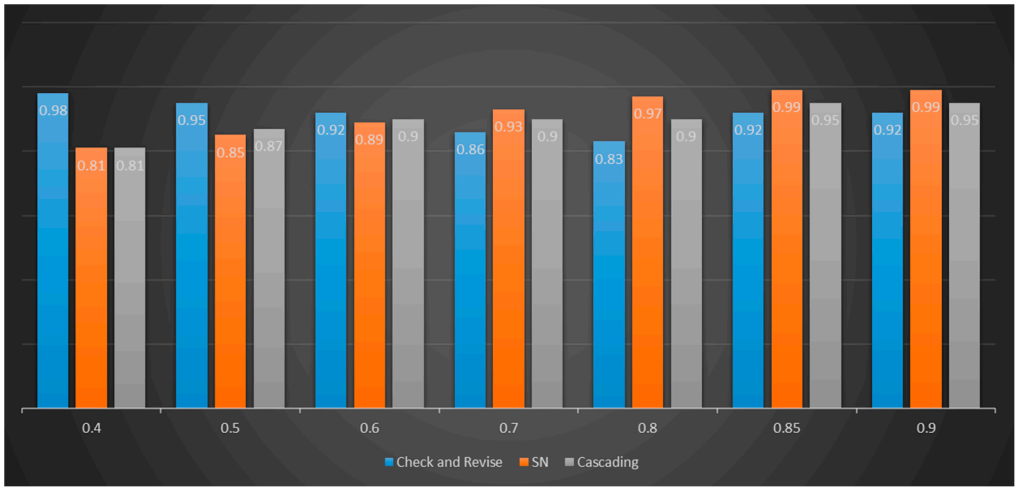

Figure 5. Values of accuracy with different Thresholds.

4. Results

We assessed the cascading model performance by comparing it with a traditional SN scheme model, whose effectiveness in recognizing some volcanic thermal features in satellite images was already proven [24]. The evaluation of scene classification models can be obtained in terms of correctness by computing statistical measures, namely True Positives (TP), True Negatives (TN), False Positives (FP) and False Negatives (FN), where TP^i (True Positives) are the images predicted to belong to class i that actually do belong to that class, TN^i (True Negatives) are the images predicted to belong to class j different from class i that actually do belong to class j, FP^i (False Positives) are the images incorrectly predicted to belong to class i that actually do belong to the other classes, and FN^i (False Negatives) are the images incorrectly predicted to belong to any other class than class i that actually belong to class i. The total number of images in the test set is given by the sum of TP, TN, FP and FN. These terms form the confusion matrix that can be used to describe the performance of the classifiers (Table 2). The confusion matrices for both models are shown in Table 3. The dark green diagonal represents correct predictions, while the other light green cells indicate incorrect predictions (E). As shown, TP^{NVA} is the number of true positive *NVA* samples in class *NVA*, while $E_{NVA,ITA}$ is the number of samples from class *NVA* that were incorrectly classified as class *ITA*. The false negative total for the class *NVA* is the sum of $E_{ITA,NVA}$, $E_{NVA,ETA}$, $E_{NVA,CSC}$, which indicates the sum of all class N samples that were incorrectly classified as class *ITA*, *ETA*, and *CSC*. False positive for any predicted class which is located in a row represents the sum of all errors in that row. Moreover, in Table 4 shown a confusion matrix for a multi-class classification in only the SqueezeNet case.

Table 2. Confusion matrix for a multi-class classification in the cascading case.

CASCADING		Real Values			
		No Volcanic Activity	**Isolated Volcanic Thermal Anomalies**	**Extended Volcanic Thermal Anomalies**	**Cloudy-Sky Condition**
Predicted	**No Volcanic Activity**	**132** TP^{NVA}	7 $E_{NVA,ITA}$	6 $E_{NVA,ETA}$	2 $E_{NVA,CSC}$
	Isolated Volcanic Thermal Anomalies	7 $E_{ITA,NVA}$	**563** TP^{ITA}	8 $E_{ITA,ETA}$	16 $E_{ITA,CSC}$
	Extended Volcanic Thermal Anomalies	0 $E_{ETA,NVA}$	9 $E_{ETA,ITA}$	**132** TP^{ETA}	0 $E_{ETA,CSC}$
	Cloudy-Sky Condition	7 $E_{CSC,NVA}$	17 $E_{CSC,ITA}$	4 $E_{CSC,ETA}$	**584** TP^{CSC}

Table 3. Performance evaluation of SqueezeNet vs Cascading.

	Precision		**Recall**		**F1-Score**	
	SN	**CASCADING**	**SN**	**CASCADING**	**SN**	**CASCADING**
No Volcanic Activity	0.48	0.90	0.74	0.90	0.58	0.90
Isolated Volcanic Thermal Anomalies	0.90	0.95	0.59	0.94	0.71	0.95
Extended Volcanic Thermal anomalies	0.92	0.94	0.87	0.88	0.89	0.91
Cloudy-Sky Condition	0.81	0.95	0.99	0.97	0.89	0.96

Table 4. Confusion matrix for a multi-class classification in the SqueezeNet case.

SN		Real Values			
		No Volcanic Activity	**Isolated Volcanic Thermal Anomalies**	**Extended Volcanic Thermal Anomalies**	**Cloudy-Sky Condition**
Predicted	**No Volcanic Activity**	**108** TP^{NVA}	109 $E_{NVA,ITA}$	1 $E_{NVA,ETA}$	6 $E_{NVA,CSC}$
	Isolated Volcanic Thermal Anomalies	29 $E_{ITA,NVA}$	**353** TP^{ITA}	8 $E_{ITA,ETA}$	3 $E_{ITA,CSC}$
	Extended Volcanic Thermal Anomalies	0 $E_{ETA,NVA}$	12 $E_{ETA,ITA}$	**131** TP^{ETA}	0 $E_{ETA,CSC}$
	Cloudy-Sky Condition	9 $E_{CSC,NVA}$	122 $E_{CSC,ITA}$	10 $E_{CSC,ETA}$	**593** TP^{CSC}

The goodness of the classification for the test set was estimated using different model performance indices. The metrics used are shown in Equations (1)–(4). In particular, the F1 score was used to deal with the unbalancing issues, i.e., the different number of samples for each class. Furthermore, micro, macro and weighted F1 scores were used for the multi-class classification problem (Equations (4)–(6)). Table 5 shows the metrics for the single SN and the cascading models.

$$\text{Precision} = \frac{\text{TP}}{\text{TP} + \text{FP}} \tag{1}$$

$$\text{Recall} = \frac{\text{TP}}{\text{TP} + \text{FN}} \tag{2}$$

$$\text{F1 score} = \frac{2 * \text{TP}}{2 * \text{TP} + \text{FP} + \text{FN}} = 2 * \frac{\text{Precision} \times \text{Recall}}{\text{Precision} + \text{Recall}} \tag{3}$$

$$\text{Micro F1 score} = \frac{\text{TP} + \text{TN}}{(\text{TP} + \text{TN}) + (\text{FP} + \text{FN})} \quad (4)$$

$$\text{Macro F1 score} = \text{mean}(\text{F1score}_{NVA} + \text{F1score}_{ITA} + \text{F1score}_{ETA} + \text{F1score}_{CLD}) \quad (5)$$

$$\text{Weighted F1 score} = \frac{\sum_{i=1}^{N} w_i * \text{F1}_{\text{score}_i}}{\sum_{i=1}^{N} w_i} \quad (6)$$

Table 5. Performance metrics for SqueezeNet and cascading.

	SN	Cascading
Micro F1-Score	0.79	0.95
Macro F1-Score	0.77	0.93
Weighted F1-Score	0.80	0.95

We applied the trained model to the testing dataset for several volcanoes. Different scenarios are shown, namely when the SN is exclusively active because the confidence level was less than 0.85, and when the check and revise block was active, allowing us to adjust the SN output having low confidence level (Figures 6 and 7). Furthermore, among the not trivial study cases, we considered lava flows fragmented by clouds. This model allowed us to create time series of the cascading outcomes for each volcano showing the type of activity and the areal extension of thermal anomalies (Figures 8 and 9).

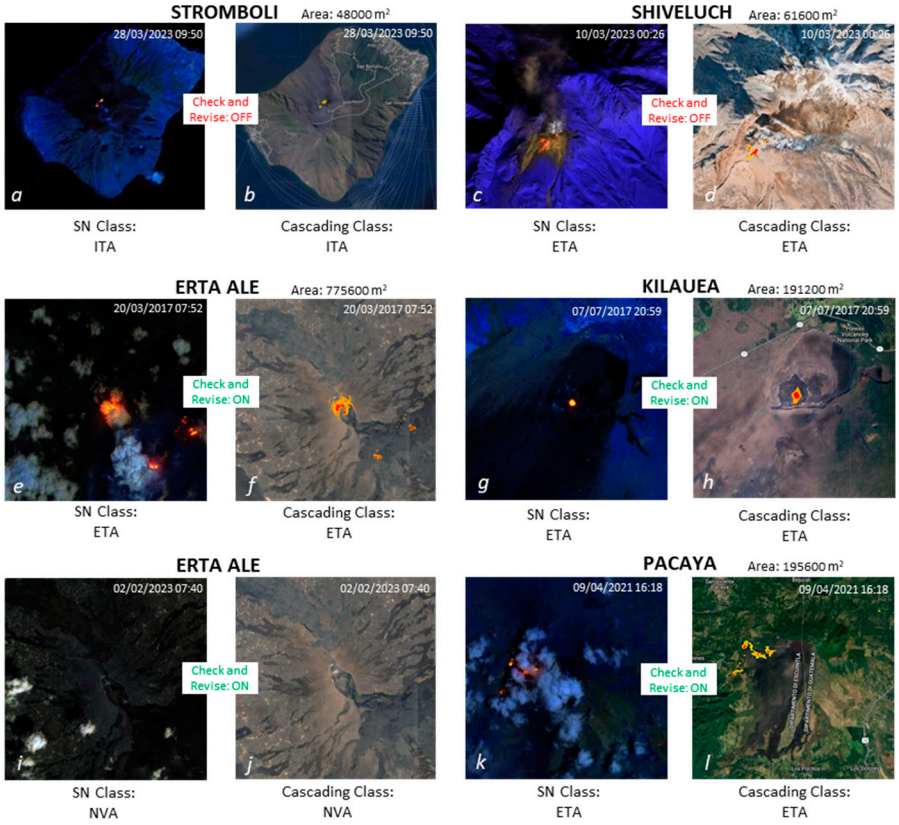

Figure 6. Cascading model study cases when check and revise block is OFF (**a**–**d**)/ON (**e**–**l**) and the cascading class corresponds to the SN output. Scenes classified using SN containing Isolated Volcanic Thermal Anomalies on Stromboli (**a**), Extended Volcanic Thermal Anomalies on Shiveluch (**c**), Extended Volcanic Thermal Anomalies on Erta Ale (**e**), Extended Volcanic Thermal Anomalies on Kilauea (**g**), No Volcanic Activity on Erta Ale (**i**), Extended Volcanic Thermal Anomalies on Pacaya (**k**), thus the corresponding cascading outcomes and area estimation using RF, (**b**,**d**,**f**,**h**,**j**,**l**) respectively.

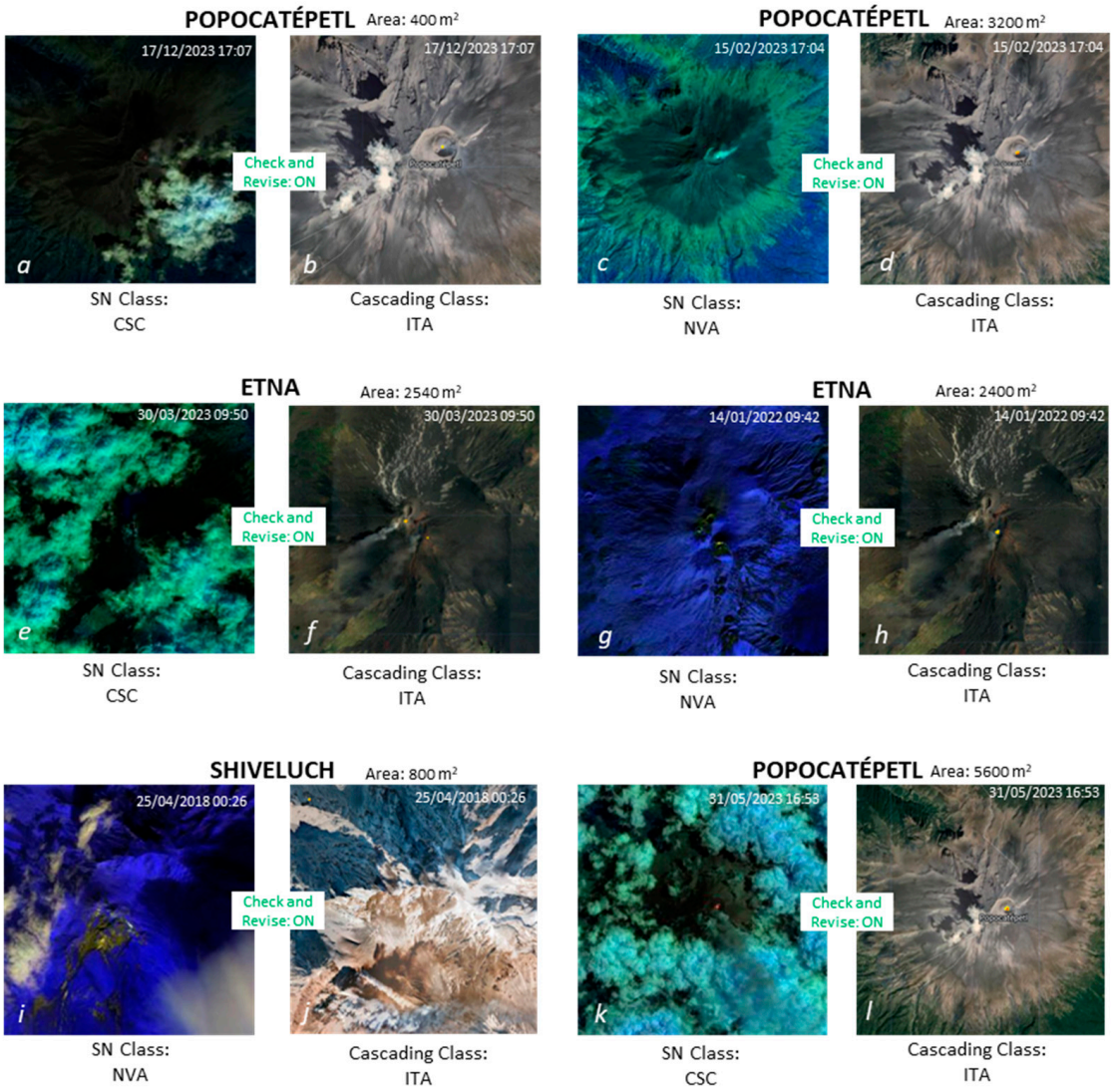

Figure 7. Cascading model study cases when check and revise block is ON, and the cascading class differs from the SN output (**a**–**l**). Scenes classified using SN containing Cloudy-Sky Condition on Popocatépetl (**a**), No Volcanic Activity on Popocatépetl (**c**), Cloudy-Sky Condition on Etna (**e**), No Volcanic Activity on Etna (**g**), No Volcanic Activity on Shiveluch (**i**), Cloudy-Sky Condition on Popocatépetl (**k**); the corresponding cascading outcomes and area estimation using RF, (**b**,**d**,**f**,**h**,**j**,**l**) respectively.

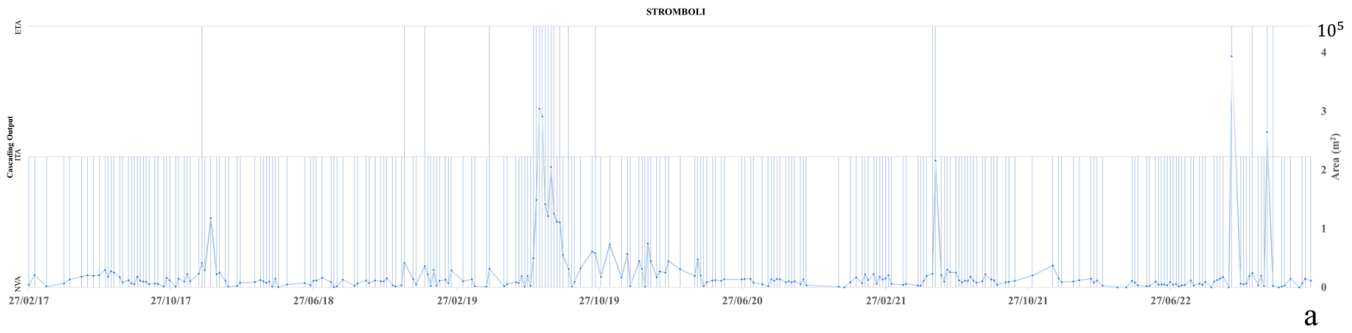

Figure 8. *Cont.*

Figure 8. Time series of volcanoes' activity: Stromboli (**a**), Etna (**b**), Ambrym (**c**), Cumbre Vieja (**d**), Erta Ale (**e**).

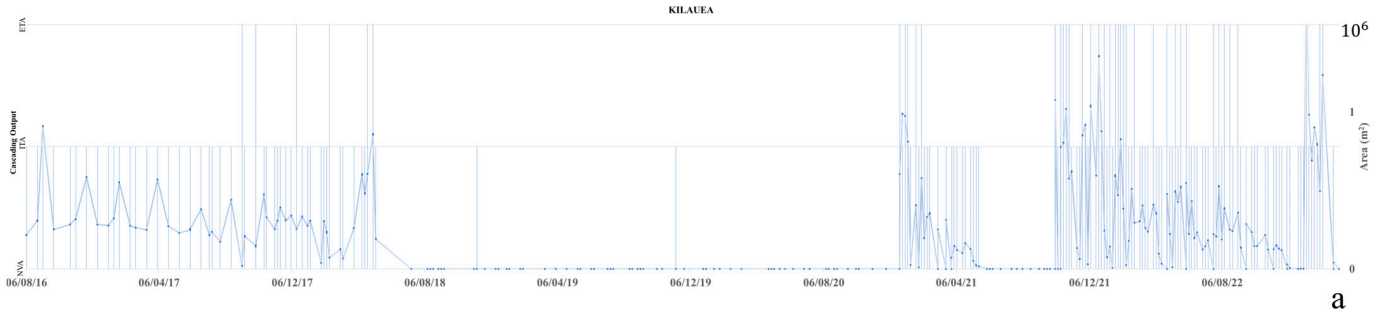

Figure 9. *Cont.*

Figure 9. Time series of volcanoes' activity: Kilauea (**a**), Klyuchevskaya (**b**), Pacaya (**c**), Popocatepetl (**d**), Shiveluch (**e**).

5. Discussion

5.1. Cascading Model Performance

The cascading approach combining SN and RF models greatly outperformed the SN model alone, reaching the highest overall accuracy of 0.95 with respect to 0.80 (Table 5). Considering all the performance metrics for each class, it is worth noting that the cascading model overall classified all the classes with accuracy greater than 0.90. The lowest performance was achieved with the '*NVA*' class mainly because of a slight underestimation tendency of the cascading, shown by a higher precision than the F1 score. This is consistent with the fact that the '*ITA*' class had a slight overestimation tendency as the metrics show, namely a recall slightly greater than the F1 score. This is due to the fact that the cascading outcome could be affected by false positive pixel detection when the check and revise block was active. Although the model worked well overall, an error that could occur was due to false positives detected by the RF, since even an isolated pixel detected led to the change of the SN outcome class. However, it is worth noting that every segmentation model had a

prediction error; thus, this was expected to happen, but since RF has a high accuracy of more than 0.90 [13], this was a rare case. The SN learned well in classifying '*ETA*' and '*CSC*' scenes, namely an F1 score greater than 0.87, while it tended to had a higher percentage of underestimated '*ITA*' scenes, i.e., where small anomalies were present. This was shown by a precision score greater than its F1 score; in fact, these scenes were misclassified mainly as both '*NVA*' and '*CSC*' and were characterized by an overestimation shown as a recall index greater than F1 score (Table 3). Figures 6 and 7 show some of the significant study cases. When only the SN model was active (Figure 6a–d), it meant that the SN outcome had a high confidence level; thus, the RF was only used to move from a general description of the identified scene to a detailed spatial mapping in both the '*ITA*' and '*ETA*' classes. In Figure 6, it can be observed that once the scene had been classified as either '*ITA*' in Stromboli (Figure 6a) or '*ETA*' in Shiveluch (Figure 6c), the images were segmented via RF (Figure 6b,d) to quantify the spatial extension of the detected anomalies (in square meters). When the confidence level was lower than the threshold, the SN outcome underwent the check and revise process that could confirm or not the SN outcome (Figure 6e–l). These were the cases for Kilauea, showing a lava lake correctly recognized as '*ETA*' and segmented (Figure 6g,h), and an absence of activity for Erta Ale (Figure 6i,l). An interesting study case was represented by a lava flow partially cooling or/and covered by clouds. It is worth noting that even lava flows fragmented by clouds were correctly classified as effusive activity by the cascading algorithm. The SN model seemed to perform generally well; however, it might have performed poorly if weak anomalies were present since it relies on a unique label encompassing the entire scene in one piece of information. In such cases, the confidence level was low and the pixel-based information provided by RF allowed us to catch small spatial features otherwise missed by the SN. This is shown in Figure 7, where both clear and cloudy scenes with very weak anomalies were wrongly classified by SN. Scenes wrongly classified as '*CSC*' by the SN for Popocatèpetl (Figure 7a,b,k,l) and Etna volcanoes (Figure 7e,f) were adjusted to '*ITA*' thanks to the use of the cascading. Similarly, the cascading correctly classified scenes as '*ITA*' otherwise recognized as '*NVA*' by the SN for Popocatèpetl (Figure 7c,d), Etna volcanoes (Figure 7g,h) and Shiveluch (Figure 7i-j). The use of the two cascading machine learning models on the entire time series of Sentinel-2 images also allowed us to follow the evolution of eruptive activity and to quantify the areas covered by thermal emissions for each monitored volcano. Figures 8 and 9 show both the type of activity and the estimated covered area for all the volcanoes from 2016 to 2023. For the sake of clarity, only values associated to the cascading output 0 to 2 are shown; cloudy scenes are not shown except from Ambrym, with most of the scenes classified as cloudy (Figure 8c). The cascading model could reveal volcanic behaviors such as the change from the rest phase to the active phase, as in Cumbre Vieja (Figure 8d) and from active to rest to active again, as in Kilauea (Figure 9a; the frequency of the effusive activity for each volcano, i.e., Etna, Klyuchevskoi, Kilauea and Shiveluch, which were particularly active (Figures 8b and 9a,b,e); the persistent Strombolian activity of Stromboli (Figure 8a) and the persistent degassing activity of Popocatepetl (Figure 9d). We were able to characterize the eruptive events in time and space by combining the cascading models with the quantification process.

5.2. Quantitative Analysis and Classification of Volcanic Thermal Activity on Target Volcanoes

Stromboli is characterized by persistent explosive activity (Figure 8a) that can sometimes turn into more intense events, producing major explosions or paroxysmal events [36,37]. These can erupt as lava flows, such as in summer 2019, when two paroxysm events occurred [16]; in this case, the cascading algorithm detected a hot area of 273,600 m^2 on 22 July 2019. A new eruptive activity began in October 2022, and this was anticipated from an increase in the areal coverage of the thermal emissions starting from 9 September 2022. The first emplaced lava flow was recognized by the cascading algorithm on 4 October 2022, estimating a hot area of about 55,000 m^2.

Over the past two decades, the eruptive activity of Etna has been characterized by persistent degassing and a frequent intertwining of explosive and effusive eruptions from its four summit craters (Figure 8b). Thus, identifying the active craters and quantifying intra-crater budget emissions in terms of areal coverage of thermal anomalies can unveil interesting scenarios associated with volcano dynamics (Figure 10). We drew in GEE the outlines geometry of each crater region and computed the contribution of each crater to the overall detected thermal anomalies; a circular area around each crater is considered, namely South-East (SE), North-East (NE), Bocca Nuova (BN) and Voragine (VOR). From February to March 2017, an eruptive phase started, leading to a lava flow emission on 15 March 2017 from the SE crater [38]. This is clearly visible in Figure 10b where the SE crater starts a consistent increase in thermal activity from January 2017. Moreover, from July 2018, we observe a growth of the areal coverage of the thermal anomalies inside the BN crater region (Figure 10c) until 26 December 2018, when Etna erupted again (between 24 and 27 December 2018) from a fissure that opened on the high south-eastern flank, generating a lava flow [7].

A new period of intense eruptive activity began on 14 December 2022 with the first of 66 paroxysms producing several lava flows [39], i.e., maximum area quantified being 1,800,000 m^2 on 18 December. All the craters show consistent increases in the areal coverage of thermal anomalies before the first paroxysm (Figure 10) with NE and SE (Figure 10a,b) starting in June 2020. Lately, from nearly June 2022, the most active crater has been BN. It is worth stating that each crater region may contain thermal anomalies associated with the emitted lava flows, thus contributing to the total area shown in Figure 10. This is especially true for SE crater, whose peak reaches higher values when lava flows are emplaced, e.g., February 2021 lava flows (Figure 10b).

The time series of the Ambrym volcano, which is primarily cloudy, is shown to highlight how the cascading model works during bad weather conditions (Figure 8c). Due to total/partial cloudiness, it is not possible to discriminate well between thermal anomalies and effusive activity, so a direct consequence can be overestimation or underestimation of the real anomaly, as well as an uncertainty in the predicted class. We investigate the Ambrym volcano's activity between January 2017 and December 2019, because clouds strongly affected the target area after this period. Major increments in the values were recorded in 2018, when the areal coverage of the thermal anomaly extended above 300,000 m^2 on 25 November and 15 December 2018 [40]. Although meteorological clouds and a potential degassing plume partially hampered the scene on June 8, it was still feasible to determine from satellite images that both craters displayed signs of the lava lake with a total hot spot area of 214,400 m^2. Instead, in the absence of cloudiness, it is possible to see three different peaks on 13 July 2018 (376,400 m^2), 25 November 2018 (343,600 m^2), and 15 December 2018 (384,000 m^2).

In Figure 8d, the start of the eruptive activity of Cumbre volcano lasting about three months in October 2021 is clearly shown. On 19 September 2021, a new eruption began from the SW flank, and the first image available from satellite on 20 September is unable to fully quantify the lava flow (552,400 m^2) due to the partial cloud cover. Two fissures opened, and multiple vents produced lava fountains, flows, and ash plumes; the flows traveled over 5 km to the west toward the coastline, eventually extending further into the ocean, damaging buildings and crops. On 30 September, we visualized and quantified the entire active lava flow (6,672,400 m^2). Strong lava effusion persisted during the first half of the month, some of which continued to feed the lava deltas on the coast.

In Figure 8e, it is possible to observe the main effusive activity between January 2017 and January 2018 that took place at Erta Ale from 2016. In this period, intense activity was characterized by two large spikes due to changes in intensity and location of the volcanic activity that coincides with the opening of new SE flank fissure vents. In particular, from 16 to 19 January 2017, ~1 km long lava flows within the summit caldera (with active lava flow area 1,466,400 m^2) were emplaced. A fissure also opened at about ~3 km from the SE crater, where a lava lake appeared on 21 January 2017 (i.e., 250,400 m^2), producing the

highest level of SO_2 emissions at Erta Ale ever observed from space [41]. From 29 April to 5 May, the new SE Rift Zone extended several kilometers to the NE, which corresponds to the highest peak in terms of area extension, namely 1,122,000 m^2 on 9 May 2017.

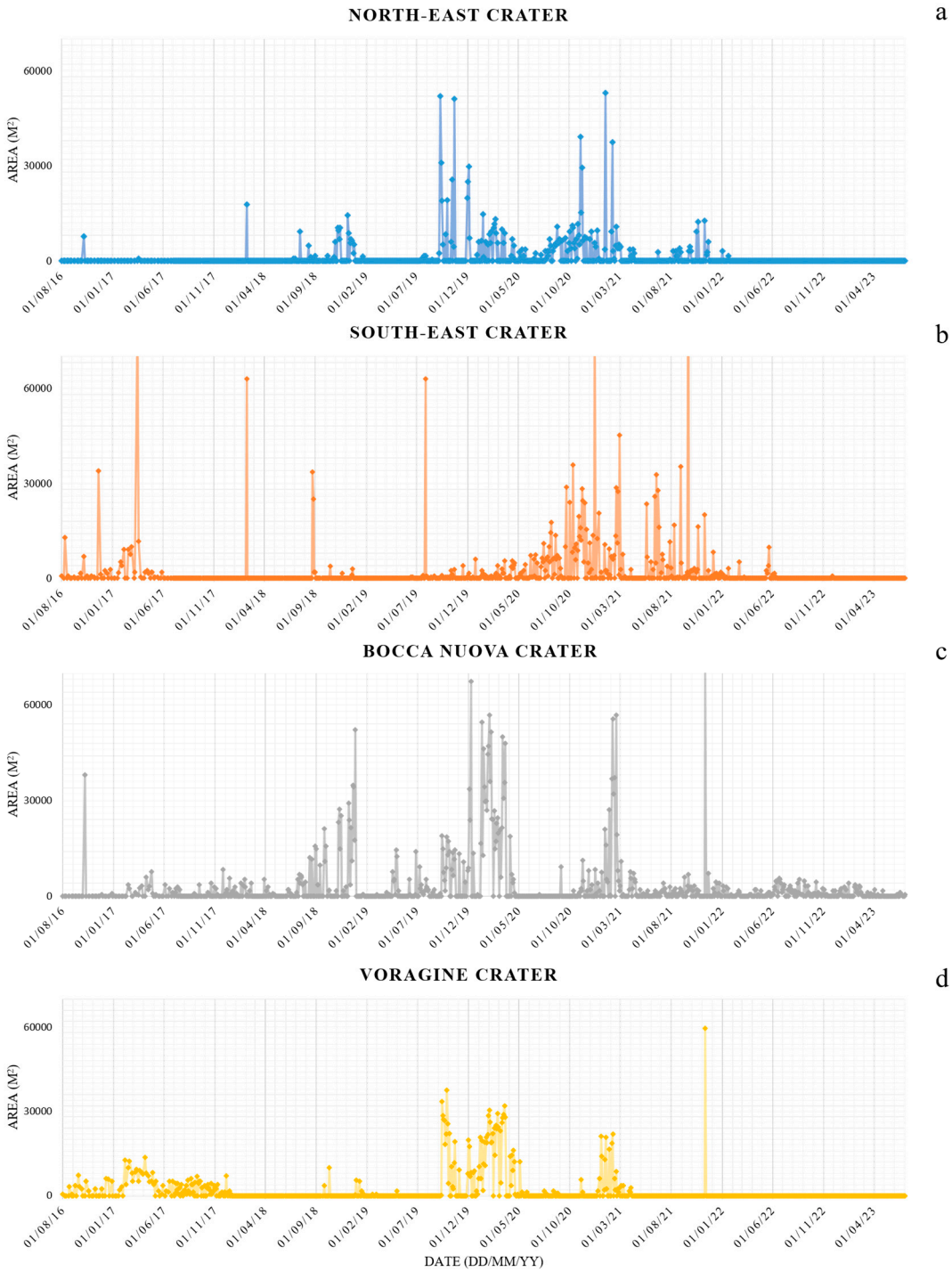

Figure 10. Contribution of different craters' activity: North-East (NE) crater (**a**), South-East (SE) crater (**b**), Bocca Nuova (BN) crater (**c**), and Voragine (VOR) crater (**d**).

Kilauea erupted almost continuously from 1983 to 2018, and again from 2020 onward. Figure 9a shows 'NVA' during this resting phase, except for two false positives detected on 9 November of the years 2018 and 2019. Interestingly, these detections occurred at the same time of the year, and they were related to human activities. Moreover, from January

to May 2021, it was possible to appreciate the transition from lava lake (i.e., 877,200 m^2) to intra-crater activity (i.e., 47,200 m^2). The almost persistent activity of varying intensities of Kilauea from October 2021 to May 2022 continued through November 2022, although thermal intensities diminished after mid-June 2022.

Figure 9b shows the time series of Klyuchevskoy from January 2020 to March 2021. On 11 January 2020, incandescence and degassing were visible, so Strombolian activity continued throughout February, with occasional explosions detected by the model as thermal anomalies. On 18 April, a lava flow began moving down the SE flank (227,200 m^2), which continued throughout April and May with sustained Strombolian and intermittent Vulcanian activity at the summit. This is clearly shown in Figure 9b by the alternate presence of both '*ITA*' and '*ETA*' in that period. Moderate explosive–effusive activity occurred on 8 June 2020 (e.g., 1 July 289,600 m^2), with Strombolian explosions, and an active lava flow. Activity from July through September was relatively low, with no thermal activity detected until a new eruptive phase began in October when activity intensified and was characterized by strong explosions, collapses of the sides of the drainage, strong thermal anomalies, and ash plumes that extended over 200 km SE from the crater; the lava flow remained active and continued to descend the SE flank. On 28 November 2021, the hot spot area was estimated 1,785,200 m^2.

In Figure 9c, we can observe the time series of Pacaya, where the period between 2019 and 2021 shows an intense activity in correspondence with the opening of flank fissures, which were the source of multiple kilometer-long lava flows. A significant increase in both effusive and explosive activity that began in February 2021 continued through mid-May, decreasing later that month. Effusive activity increased significantly during March 2021; by early in the month, as many as three lava flows with multiple branches, all about 1 km long, were simultaneously active on multiple flanks. A new fast-moving flow appeared on the SW flank during the second half of March and rapidly reached 1.5 km in length, ultimately extending over 3 km. A new flow emerged along a similar path at the end of April and grew to over 2 km long in early May before activity at its source fissure ended on 17 May. In particular, we can see a peak on 5 March 2021 (152,440 m^2), where two main flows with multiple branches extended 300–500 m down the S flank of Pacaya, causing very bright thermal signatures in satellite imagery in absence of cloudiness.

The time series of Popocatépetl is mainly characterized by '*ITA*' class (Figure 9d). During 16–23 May, the activity at Popocatépetl intensified as a consequence of lava dome formation, growth and subsequent destruction. Steam, gas and ash emissions were continuous with occasional ejections of incandescent material at short distances onto the flanks. On 21 May, the activity increased thus the National Coordination of Civil Protection in Mexico updated the Popocatépetl Volcano Alert to yellow (phase 3). Once the volcanic activity became intense, '*ETA*' class was recognized by the cascading model estimating an area of 845,600 m^2, probably due to lava effusions that piled up into domes but that were soon blown apart in the occasional blasts, thanks to the high gas content in this new batch of magma.

In Figure 9e, it is possible to observe the time series of Shiveluch, in particular the period corresponding to the growth of the lava dome and its subsequent collapse. During July 2022, the volcanic activity consisted of lava dome growth, explosions accompanied by hot avalanches, ash plumes, incandescence from the lava dome, and strong fumarolic activity. The lava dome continued to grow until 5–7 September and finally, on 31 October (111,200 m^2), it collapsed, producing avalanches and ash plumes. November and December saw new lava dome growth, incandescence, explosions, and strong fumarolic activity, and this activity lasted until January 2023.

6. Conclusions

We demonstrated the potential of the cascading pipeline for classifying high-temperature volcanic features and quantifying the spatial extension of thermal anomalies in high-spatial resolution satellite data (Sentinel-2 MultiSpectral Instrument, S2-MSI). The

ability to combine two separate machine learning models—a scene classifier and a pixel-based segmentation model—into a 'top-down' cascading architecture makes this method highly effective, achieving an accuracy of 95%. These findings illustrate how the cascading technique can be used to fully characterize any S2-MSI satellite image in almost real time, offering valuable assistance in the mapping, monitoring, and characterization of volcanic thermal features. Therefore, the prompt use of the trained model enables the qualitative assessment of the threat posed by volcanic eruptions worldwide. Scenes classified as isolated thermal anomalies associated with volcanic events that are spatially confined in the summit area of the volcano do not represent an immediate threat to people living nearby. Moreover, scenes classified as extended thermal anomalies related to volcanic events whose eruptive products might reach inhabited areas may pose a serious threat. Finally, the model's high level of accuracy enabled the detection of thermal signals that are often challenging to pick up with current detectors. Spatially characterizing the detected thermal anomalies allows to both highlight significant pre-eruptive thermal changes and estimate the areal coverage of the erupted products. Combining multiple models allowed us to create better and more powerful predictors, making this tool suitable for near-real time volcanic activity detection. Next steps will be focused on merging the retrieved time series information to catch temporal hidden patterns unveiling volcano dynamics.

Supplementary Materials: The following supporting information can be downloaded at: https://www.mdpi.com/article/10.3390/rs16010171/s1.

Author Contributions: Conceptualization, C.C. and S.C.; methodology, C.C. and S.C.; software, C.C. and S.C.; validation, F.T. and C.D.N.; formal analysis, F.T.; investigation, C.C. and S.C.; resources, C.D.N.; data curation, F.T.; writing—original draft preparation, S.C.; writing—review and editing, C.C and C.D.N.; visualization, F.T.; supervision, C.C. and C.D.N.; project administration, C.C. and C.D.N.; funding acquisition, C.D.N. All authors have read and agreed to the published version of the manuscript.

Funding: This research was partially funded by both Project FIRST—ForecastIng eRuptive activity at Stromboli volcano: timing, eruptive style, size, intensity, and duration, INGV—Progetto Strategico Dipartimento Vulcani 2019 (Delibera n. 144/2020) and project INGV—Pianeta Dinamico VT_ORME 2023-2025, (OB.FU. 1020.010).

Data Availability Statement: The dataset used to train the SN is available as Supplementary Material.

Acknowledgments: This work was developed within the framework of the Laboratory of Technologies for Volcanology (TechnoLab) at the INGV in Catania (Italy). We thank Stephen Conway for revising the English of the manuscript.

Conflicts of Interest: The authors declare no conflict of interest.

References

1. Rothery, D.A.; Francis, P.W.; Wood, C.A. Volcano Monitoring Using Short Wavelength Infrared Data from Satellites. *J. Geophys. Res. Solid Earth* **1988**, *93*, 7993–8008. [CrossRef]
2. Harris, A. *Thermal Remote Sensing of Active Volcanoes: A User's Manual*; Cambridge University Press: Cambridge, UK, 2013; ISBN 978-0-521-85945-5.
3. Ganci, G.; Cappello, A.; Bilotta, G.; Del Negro, C. How the Variety of Satellite Remote Sensing Data over Volcanoes Can Assist Hazard Monitoring Efforts: The 2011 Eruption of Nabro Volcano. *Remote Sens. Environ.* **2020**, *236*, 111426. [CrossRef]
4. Oppenheimer, C.M.M.; Rothery, D.A. Infrared Monitoring of Volcanoes by Satellite. *J. Geol. Soc.* **1991**, *148*, 563–569. [CrossRef]
5. Harris, A.J.L.; Flynn, L.P.; Dean, K.; Pilger, E.; Wooster, M.; Okubo, C.; Mouginis-Mark, P.; Garbeil, H.; Thornber, C.; De la Cruz-Reyna, S.; et al. Real-Time Satellite Monitoring of Volcanic Hot Spots. *Wash. DC Am. Geophys. Union Geophys. Monogr. Ser.* **2000**, *116*, 139–159. [CrossRef]
6. Francis, P.; Rothery, D. Remote Sensing of Active Volcanoes. *Annu. Rev. Earth Planet. Sci.* **2000**, *28*, 81–106. [CrossRef]
7. Corradino, C.; Ganci, G.; Cappello, A.; Bilotta, G.; Hérault, A.; Del Negro, C. Mapping Recent Lava Flows at Mount Etna Using Multispectral Sentinel-2 Images and Machine Learning Techniques. *Remote Sens.* **2019**, *11*, 1916. [CrossRef]
8. Steffke, A.M.; Harris, A.J.L. A Review of Algorithms for Detecting Volcanic Hot Spots in Satellite Infrared Data. *Bull. Volcanol.* **2011**, *73*, 1109–1137. [CrossRef]

9. Wright, R.; Flynn, L.P.; Garbeil, H.; Harris, A.J.L.; Pilger, E. MODVOLC: Near-Real-Time Thermal Monitoring of Global Volcanism. *J. Volcanol. Geotherm. Res.* **2004**, *135*, 29–49. [CrossRef]
10. Higgins, J.; Harris, A. VAST: A Program to Locate and Analyse Volcanic Thermal Anomalies Automatically from Remotely Sensed Data. *Comput. Geosci.* **1997**, *23*, 627–645. [CrossRef]
11. Goodfellow, I.; Bengio, Y.; Courville, A. *Deep Learning*; MIT Press: Cambridge, MA, USA, 2016; ISBN 978-0-262-33737-3.
12. Bonaccorso, G. *Machine Learning Algorithms*; Packt Publishing Ltd.: Birmingham, UK, 2017; ISBN 978-1-78588-451-1.
13. Corradino, C.; Amato, E.; Torrisi, F.; Del Negro, C. Data-Driven Random Forest Models for Detecting Volcanic Hot Spots in Sentinel-2 MSI Images. *Remote Sens.* **2022**, *14*, 4370. [CrossRef]
14. Kato, S.; Miyamoto, H.; Amici, S.; Oda, A.; Matsushita, H.; Nakamura, R. Automated Classification of Heat Sources Detected Using SWIR Remote Sensing. *Int. J. Appl. Earth Obs. Geoinf.* **2021**, *103*, 102491. [CrossRef]
15. Del Negro, C.; Amato, E.; Corradino, C.; Torrisi, F.; Ramsey, M.S. Volcano Hazard Monitoring at Mount Etna Using Multispectral Satellite Imagery and Artificial Intelligence. In Proceedings of the AGU Fall Meeting, Chicago, IL, USA, 12–16 December 2022.
16. Corradino, C.; Amato, E.; Torrisi, F.; Calvari, S.; Del Negro, C. Classifying Major Explosions and Paroxysms at Stromboli Volcano (Italy) from Space. *Remote Sens.* **2021**, *13*, 4080. [CrossRef]
17. Torrisi, F.; Amato, E.; Corradino, C.; Mangiagli, S.; Del Negro, C. Characterization of Volcanic Cloud Components Using Machine Learning Techniques and SEVIRI Infrared Images. *Sensors* **2022**, *22*, 7712. [CrossRef] [PubMed]
18. Corradino, C.; Ramsey, M.S.; Pailot-Bonnétat, S.; Harris, A.J.L.; Negro, C.D. Detection of Subtle Thermal Anomalies: Deep Learning Applied to the ASTER Global Volcano Dataset. *IEEE Trans. Geosci. Remote Sens.* **2023**, *61*, 1–15. [CrossRef]
19. Gama, J.; Brazdil, P. Cascade Generalization. *Mach. Learn.* **2000**, *41*, 315–343. [CrossRef]
20. Mahataa, K.; Sarkarb, A.; Dasb, R.; Dasb, S. Land Use Land Cover Classification by Applying Ensemble Approaches on Multi Temporal Remote Sensing Images. *Int. J. Manag. Technol. Eng.* 2019. Available online: https://www.researchgate.net/publication/332174353_Land_Use_Land_Cover_Classification_by_applying_Ensemble_Approaches_on_Multi_Temporal_Remote_Sensing_Images (accessed on 17 October 2023).
21. Aziz, A.A.; Indahwati; Sartono, B. Improving Prediction Accuracy of Classification Model Using Cascading Ensemble Classifiers. *IOP Conf. Ser. Earth Environ. Sci.* **2019**, *299*, 012025. [CrossRef]
22. Ray, S.; De Sarkar, A. Execution Analysis of Load Balancing Algorithms in Cloud Computing Environment. *Int. J. Cloud Comput. Serv. Archit. (IJCCSA)* **2012**, *2*, 1–13.
23. Sether, A. Cloud Computing Benefits 2016. 2016. Available online: https://papers.ssrn.com/sol3/papers.cfm?abstract_id=2781593 (accessed on 17 October 2023).
24. Amato, E.; Corradino, C.; Torrisi, F.; Del Negro, C. A Deep Convolutional Neural Network for Detecting Volcanic Thermal Anomalies from Satellite Images. *Remote Sens.* **2023**, *15*, 3718. [CrossRef]
25. Gorelick, N.; Hancher, M.; Dixon, M.; Ilyushchenko, S.; Thau, D.; Moore, R. Google Earth Engine: Planetary-Scale Geospatial Analysis for Everyone. *Remote Sens. Environ.* **2017**, *202*, 18–27. [CrossRef]
26. Carneiro, T.; Medeiros Da NóBrega, R.V.; Nepomuceno, T.; Bian, G.-B.; De Albuquerque, V.H.C.; Filho, P.P.R. Performance Analysis of Google Colaboratory as a Tool for Accelerating Deep Learning Applications. *IEEE Access* **2018**, *6*, 61677–61685. [CrossRef]
27. Enhanced Volcanic Hot-Spot Detection Using MODIS IR Data: Results from the MIROVA System—Geological Society, London, Special Publications. Available online: https://www.lyellcollection.org/doi/full/10.1144/SP426.5 (accessed on 17 October 2023).
28. Eesa, A.S.; Arabo, W.K. A Normalization Methods for Backpropagation: A Comparative Study. *Sci. J. Univ. Zakho* **2017**, *5*, 319–323. [CrossRef]
29. Iandola, F.N.; Han, S.; Moskewicz, M.W.; Ashraf, K.; Dally, W.J.; Keutzer, K. SqueezeNet: AlexNet-Level Accuracy with 50× Fewer Parameters and <0.5 MB Model Size. *arXiv* **2016**, arXiv:1602.07360.
30. Lee, H.J.; Ullah, I.; Wan, W.; Gao, Y.; Fang, Z. Real-Time Vehicle Make and Model Recognition with the Residual SqueezeNet Architecture. *Sensors* **2019**, *19*, 982. [CrossRef] [PubMed]
31. Deng, J.; Dong, W.; Socher, R.; Li, L.-J.; Li, K.; Fei-Fei, L. ImageNet: A Large-Scale Hierarchical Image Database. In Proceedings of the 2009 IEEE Conference on Computer Vision and Pattern Recognition, Miami, FL, USA, 20–25 June 2009; pp. 248–255.
32. Huang, J.; Lu, X.; Chen, L.; Sun, H.; Wang, S.; Fang, G. Accurate Identification of Pine Wood Nematode Disease with a Deep Convolution Neural Network. *Remote Sens.* **2022**, *14*, 913. [CrossRef]
33. Lin, W.; Wu, Z.; Lin, L.; Wen, A.; Li, J. An Ensemble Random Forest Algorithm for Insurance Big Data Analysis. *IEEE Access* **2017**, *5*, 16568–16575. [CrossRef]
34. Belgiu, M.; Drăguţ, L. Random Forest in Remote Sensing: A Review of Applications and Future Directions. *ISPRS J. Photogramm. Remote Sens.* **2016**, *114*, 24–31. [CrossRef]
35. Paul, A.; Mukherjee, D.P.; Das, P.; Gangopadhyay, A.; Chintha, A.R.; Kundu, S. Improved Random Forest for Classification. *IEEE Trans. Image Process.* **2018**, *27*, 4012–4024. [CrossRef]
36. Giudicepietro, F.; Calvari, S.; D'Auria, L.; Traglia, F.D.; Layer, L.; Macedonio, G.; Caputo, T.; Cesare, W.D.; Ganci, G.; Martini, M.; et al. Variations of Stromboli Activity Related to the 2019 Paroxysmal Phase Revealed by SOM Clustering of Seismo-Acoustic Data and Its Comparison with Video Recordings and GBInSAR Measurements. In Proceedings of the EGU General Assembly, Vienna, Austria, 23–27 May 2022.

37. Calvari, S.; Di Traglia, F.; Ganci, G.; Bruno, V.; Ciancitto, F.; Di Lieto, B.; Gambino, S.; Garcia, A.; Giudicepietro, F.; Inguaggiato, S.; et al. Multi-Parametric Study of an Eruptive Phase Comprising Unrest, Major Explosions, Crater Failure, Pyroclastic Density Currents and Lava Flows: Stromboli Volcano, 1 December 2020–30 June 2021. *Front. Earth Sci.* **2022**, 10. [CrossRef]
38. Cappello, A.; Ganci, G.; Bilotta, G.; Hérault, A.; Zago, V.; Del Negro, C. Satellite-Driven Modeling Approach for Monitoring Lava Flow Hazards during the 2017 Etna Eruption. *Ann. Geophys.* **2019**, *62*. [CrossRef]
39. Amato, E. Machine Learning and Best Fit Approach to Map Lava Flows from Space. *Il Nuovo C. C.* **2022**, *45*, 1–12.
40. Marchese, F.; Pergola, N.; Telesca, L. Investigating the Temporal Fluctuations in Satellite Advanced Very High Resolution Radiometer Thermal Signals Measured in the Volcanic Area of Etna (Italy). *Fluct. Noise Lett.* **2006**, *6*, L305–L316. [CrossRef]
41. Moore, C.; Wright, T.; Hooper, A.; Biggs, J. The 2017 Eruption of Erta 'Ale Volcano, Ethiopia: Insights Into the Shallow Axial Plumbing System of an Incipient Mid-Ocean Ridge. *Geochem. Geophys. Geosyst.* **2019**, *20*, 5727–5743. [CrossRef]